

## Article

# Experimental and Numerical Study on the Bending Behavior of Satin-Woven SiC<sub>f</sub>/SiC Composites

Xiang Li <sup>1</sup> and Ruiying Luo <sup>2,\*</sup><sup>1</sup> School of Physics, Beihang University, Beijing 100191, China; lixiang2018@buaa.edu.cn<sup>2</sup> Research Institute for Frontier Science, Beihang University, Beijing 100191, China

\* Correspondence: ryluo@buaa.edu.cn

**Abstract:** The present research intends to explore the progressive failure in the case of five-harness SiC<sub>f</sub>/SiC satin-woven sheet composites consisting of twelve layers using a combination of numerical and experimental methods. For derivation and characterization of the bending behavior, a three-point bending procedure was used under conditions of atmospheric temperature. A charge-coupled device (CCD) camera was used to monitor the initiation and evolution of the failures. Variations in the strain fields were quantified following the digital image correlation (DIC) approach, whereas the resultant failure markings were elucidated by conducting microscopic assessments. The 3D finite element modeling (FEM) of the experiment was accomplished via ABAQUS/Explicit, thereby reproducing the material performance. A 3D-modified theory of the Tsai-Wu failure initiation was executed by exploiting the VUMAT subroutine. The evolutionary rule was used to study the complementary failure. A cohesive zone element of the composite interlayer was utilized to mimic the intra-deformation interfacial damage. The DIC-based experimental values of the strain fields agreed favorably with the numerical computations and the strength value error was less than 10%. An in-depth investigation was performed concerning the advantage of the 3D modeling approach to study the applicability of the method for the foreseeable distribution of the complex field parameters (e.g., progressive failure deposition and free edge effect) inside the critical specimen section.



**Citation:** Li, X.; Luo, R. Experimental and Numerical Study on the Bending Behavior of Satin-Woven SiC<sub>f</sub>/SiC Composites. *Coatings* **2022**, *12*, 780. <https://doi.org/10.3390/coatings12060780>

Academic Editor: Csaba Balázsi

Received: 25 May 2022

Accepted: 31 May 2022

Published: 6 June 2022

**Publisher's Note:** MDPI stays neutral with regard to jurisdictional claims in published maps and institutional affiliations.



**Copyright:** © 2022 by the authors. Licensee MDPI, Basel, Switzerland. This article is an open access article distributed under the terms and conditions of the Creative Commons Attribution (CC BY) license (<https://creativecommons.org/licenses/by/4.0/>).

**Keywords:** progressive damage; DIC; SiC<sub>f</sub>/SiC composite; bending test

## 1. Introduction

Satin weave silicon carbide fiber/silicon carbide (SiC<sub>f</sub>/SiC) composites play an important part in the industries. These are better than metals in terms of lifecycles and mechanical properties. In comparison, they are superior to traditional laminated composite structures in terms of damage tolerance. These materials are characterized by varying loading conditions, such as shock, vibration, and fatigue. Given the probable enhancements in the strength and stiffness of composites through modification of the yarn structure, reinforcement morphology, and volume fraction, these materials offer developers a comparatively large space for design to satisfy the specific usage requirements for specific applications.

Recently, woven composites have been well-received for their excellent mechanical performance. Dalmaz [1–3] examined the mechanical performance of the C/SiC composite via theoretical simulation plus experimentation. Wan [4] examined the applicability of light-curable resin composites reinforced by glass fabrics in the orthotic settings. Hallal [5] put forward the three-stage homogenization approach “3SHM” for the valid elasticity assessment of woven composites. In the static loading scenario, Daggumati et al. [6] accomplished local failure simulation for a satin-woven five-harness composite by utilizing a meso-SFE model. The results demonstrated early failure at the weft yarn margins, whereas during the later period, the damage was predicted by the free surface cells. Utilizing the Murakami damage tensor, Zako et al. [7] exploited the constitutive principle, where the anisotropic failure was taken into consideration. In the case of a four-directional 3D-braided composite, Fang et al. [8] modeled the course of damage progression to observe

the damage mode under the control of equivalent material displacement and fracture energy. Huhne et al. [9] comparatively studied the constant versus continuous degradation models for material constants. The results revealed that the results obtained using the latter agreed well with the experimental results. Stereo-image correlation (SIC) was adopted for evaluating the composite performance by conducting mechanical tests [10]. Experiments in [11,12] explored various woven laminar composites loaded with quasi-static tension to elucidate the failure mechanisms. Utilizing the SEM (scanning electron microscope), Lisle et al. [13] probed into the damage evolution for a thin-woven laminar composite that was loaded with tension. Such failure traits as the chief damage patterns and fiber cracks of the samples were investigated. In the literature, experimental, analytical, and numerical modeling techniques have been used to explore damage mechanisms in composites [14–18].

Extensive virtual support is possible for the design and realization of to-be-verified large composite architectures under conditions of reinforced computational capacity. Thus, through choreographed laboratory tests, high-fidelity numerical modeling technologies, which can forecast different damage patterns and their interactions attributed to local 3D layouts of stresses, should be developed to assess the structural intactness for the primary engineered components of the composites. Compared to laboratory tests, major compound components subjected to complicated operational loading conditions usually show more sophisticated damage patterns, such as matrix cracking. There have been extensive reports concerning the free edge effect in the laminar composites [19–21].

In recent decades, multiple failure theories for the prediction of damage initiation have been proposed for various composites to identify complicated damage mechanisms. Such theories of progressive damage have been reported by Tsai-Wu [22], Hashin [23,24], Puch [25], as well as Chang-Chang [26], which have been used for predicting complicated damage behavior under practical application situations.

To study the initiation of damage and its progression in satin-woven sheet composites, the DIC approach was used. Meanwhile, the dynamic full-field strain contour lines were formed. We performed a detailed microscopic examination of the fracture site to determine the failure mode. To understand the behavior of the composite specimens under loading, the 3D FE modeling was accomplished. The innovations of the paper mainly include: the model was based on the 3D Tsai-Wu criterion within an appropriate damage evolution law, where a VUMAT subroutine was exploited, the cohesive elements were used to model the delamination between layers, and this work is helpful in practical applications, including calculating the strength of composite materials and improving the preparation process of composites.

## 2. Materials and Experiment

### 2.1. Processing of the 5-Harness 12-Layer SiC<sub>f</sub>/PyC/SiC Satin-Woven Sheet Composites

Fabrication of the pyrolytic carbon (PyC) interfaced SiC<sub>f</sub>/SiC composites was accomplished via CVI (chemical vapor infiltration) and subsequent PIP (precursor infiltration pyrolysis).

In the first step, a 2D preform with approximately 30% fiber volume fractions was prepared following the 2D paving procedure, where the continuous five-satin-weave SiC fibers were utilized as the reinforcements.

Then, on the fiber surface of the preform, the C<sub>3</sub>H<sub>6</sub> (propylene) was used to coat a PyC interfacial film following the chemical vapor deposition (CVD) method at 850 °C.

The last step involved the PIP-based fabrication of the SiC matrix, where the diluent was analytical-grade xylene, and the precursor was polycarbosilane. Following the vacuum impregnation with polycarbosilane (PCS)/xylene buffer (50 wt.%), the preforms were subjected to 1 h of pyrolysis at 1000 °C. Repeated impregnation–pyrolysis cycles were performed until the gain of mass per cycle of densification was lower than 1%.

The specimens (39.9 mm L × 5.9 mm W × 2.9 mm T) used in the three-point bending procedure were severed from a big SiC<sub>f</sub>/PyC/SiC sheet composite with warp and weft lines aligned. The morphological description of the SiC<sub>f</sub>/PyC/SiC composite surfaces is presented in Figure 1.

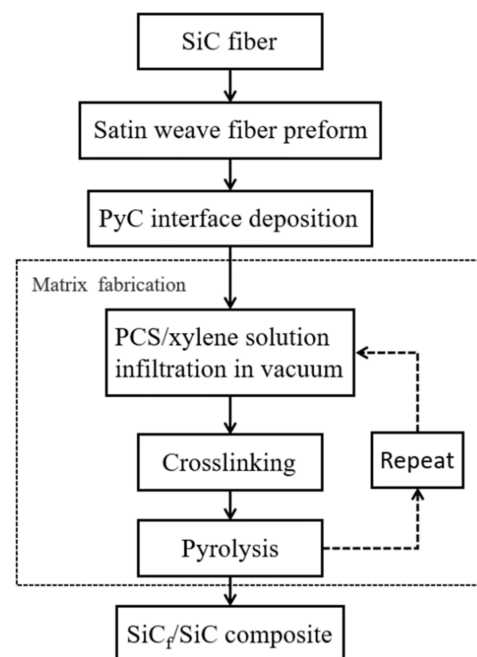


**Figure 1.** The flowchart of the material preparation.

## 2.2. Experimental Setup and Procedure

A universal electronic tester was used to implement the three-point bending procedure for the specimens (Figure 2). The tester was sufficiently qualified to provide accuracies of 0.1% for displacement control and 0.5% for force control. The rates of deformation loading in the tension experimentation were 0.4 mm/min.

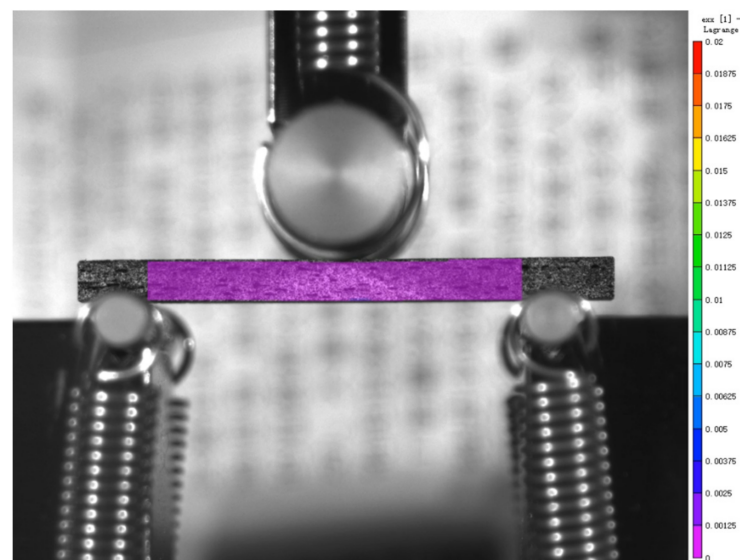


**Figure 2.** Experiment schematic.

The intra-experimental strain layout and displacement behavior of the  $\text{SiC}_t/\text{PyC}/\text{SiC}$  composites were studied. The specimen surface displacements and strain fields were examined following the 2D DIC scheme. Before the experiments were conducted, the surfaces of the specimens were sprayed with speckles. Subsequently, an imaging system was deployed at the specimen front by making the spot surface perpendicular to the camera's optical axis (Figure 3).

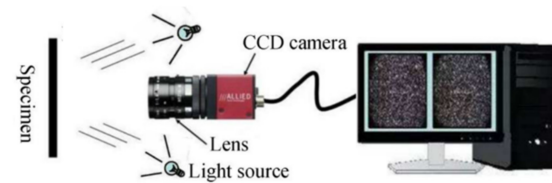


Figure 3. Strain measurement methods.

The photographing method was accomplished at a 1 Hz frequency using a CCD camera (resolution:  $2592 \times 1944$ ) with an industrial telephoto lens (focal length: 75 mm). The Vic-2D 2009 program (Correlated Solutions, Irmo, SC, USA) was used for the experiments, and the pre-deformation and post-deformation spot images were subjected to the DIC-based evaluation process under subset and step sizes of 29 and 5 pixels, respectively.

### 3. Numerical Modeling

#### 3.1. FE Model for Bending Test

As illustrated in Figure 4, for the five-harness SiCf/PyC/SiC satin-woven sheet composites consisting of twelve layers, the three-point bending procedure was modeled using 3D FEA. The quasi-static simulations were executed via ABAQUS FEA under an explicit scheme for temporal integration. The dimensions of the FE model were  $39.9 \times 5.9 \times 2.9$  mm. The meshing of the laminates was accomplished using eight-node C3D8R solid elements under conditions of hourglass control and reduced integration. The scant impact of the initial thickness on the interfacial mechanical performance was studied. We mimicked the failure behavior of the composite interface with the COH3D8 cohesive elements (zero thickness). The optimum size was finalized as 0.2 mm during the meshing analysis after considering the trade-off between computational duration and outcome accuracy. Eight-node solid elements containing complete/simplified integration and hourglass control were used.

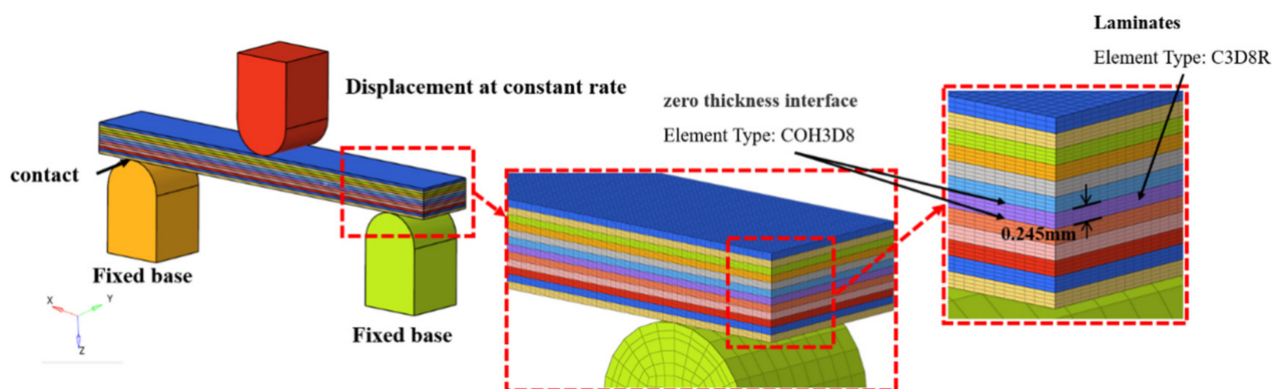


Figure 4. The 3D FE model of the 3-point bending test for 5-harness satin weave composite plates consisting of 12 layers.

Figure 4 shows the boundary situations in the case of the FE model, which can be fixed through contact between the indenter under conditions of a constant speed and the fixed-base mesh using a coarse mesh. It is restricted as a rigid body to promote computation efficiency. Additionally, a smaller friction coefficient is taken into consideration to accelerate the process of calculation convergence. The failure mechanical properties of the composite were mimicked with the progressive failure model by following the 3D Tsai-Wu criterion. The process of delamination on interfaces was mimicked through the modeling of the cohesive zone.

#### 3.2. Damage Model of the Satin Weave Composites

The satin weave composite fracture under conditions of bending load shows pseudo-plasticity. This is accompanied by yarn breakage and interface delamination. Simultane-

ously, some damage mechanisms in satin weave composites are integrated. Usually, every failure mechanism can be decomposed into the criterion of failure initiation and the law of failure progression.

Insignificant differences were noted between the mechanical properties in-plane (X- and Y-directions, as seen from Figure 5), and this could be attributed to the structural properties of the composites. The thickness direction (Z-direction) properties differed significantly from the in-plane properties.

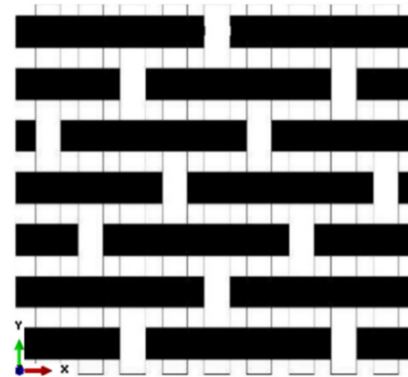


Figure 5. Five-harness satin weave composites structure.

The stress components in every direction are considered in the 3D Tsai-Wu criterion, a common scholarly practice for the damage description in the 3D interwoven composites. The Tsai-Wu criterion can be used for defining the damage initiation of the composites as follows:

$$F_{Tsai} = F_1\sigma_1 + F_2\sigma_2 + F_3\sigma_3 + F_{11}\sigma_1^2 + F_{22}\sigma_2^2 + F_{33}\sigma_3^2 + 2F_{12}\sigma_1\sigma_2 + 2F_{23}\sigma_2\sigma_3 + 2F_{31}\sigma_3\sigma_1 + F_{44}\sigma_4^2 + F_{55}\sigma_5^2 + F_{66}\sigma_6^2 = 1 \tag{1}$$

where  $F_1 = 1/Z_t - 1/Z_c$ ,  $F_2 = 1/X_t - 1/X_c$ ,  $F_3 = 1/Y_t - 1/Y_c$ ,  $F_{11} = 1/(Z_tZ_c)$ ,  $F_{22} = 1/(X_tX_c)$ ,  $F_{33} = 1/(Y_tY_c)$ ,  $F_{44} = 1/(S_{23})^2$ ,  $F_{55} = 1/(S_{13})^2$ ,  $F_{66} = 1/(S_{12})^2$ ,  $F_{12} = -\frac{1}{2}\sqrt{F_{11}F_{22}}$ ,  $F_{23} = -\frac{1}{2}\sqrt{F_{22}F_{33}}$ , and  $F_{31} = -\frac{1}{2}\sqrt{F_{33}F_{11}}$ . To allow for the steady simulations, we converted the stress,  $\sigma_i$  ( $i = 1, 2, 3, 4, 5, 6$ ), in Formula (1) into strain,  $\varepsilon_i$ , in accordance with the constitutive relationships, presented as follows:

$$\sigma_i = C_{ij}\varepsilon_j \quad (i, j = 1, 2, 3, 4, 5, 6) \tag{2}$$

Regarding the orthotropic materials, the expression for the strain-based Tsai-Wu criterion is as follows:

$$F_{Tsai} = F_1(C_{11}\varepsilon_1 + C_{12}\varepsilon_2 + C_{13}\varepsilon_3) + F_2(C_{21}\varepsilon_1 + C_{22}\varepsilon_2 + C_{23}\varepsilon_3) + F_3(C_{31}\varepsilon_1 + C_{32}\varepsilon_2 + C_{33}\varepsilon_3) + F_{11}(C_{11}\varepsilon_1 + C_{12}\varepsilon_2 + C_{13}\varepsilon_3)^2 + F_{22}(C_{21}\varepsilon_1 + C_{22}\varepsilon_2 + C_{23}\varepsilon_3)^2 + F_{33}(C_{31}\varepsilon_1 + C_{32}\varepsilon_2 + C_{33}\varepsilon_3)^2 + 2F_{12}(C_{11}\varepsilon_1 + C_{12}\varepsilon_2 + C_{13}\varepsilon_3)(C_{21}\varepsilon_1 + C_{22}\varepsilon_2 + C_{23}\varepsilon_3) + 2F_{23}(C_{21}\varepsilon_1 + C_{22}\varepsilon_2 + C_{23}\varepsilon_3)(C_{31}\varepsilon_1 + C_{32}\varepsilon_2 + C_{33}\varepsilon_3) + 2F_{31}(C_{31}\varepsilon_1 + C_{32}\varepsilon_2 + C_{33}\varepsilon_3)(C_{11}\varepsilon_1 + C_{12}\varepsilon_2 + C_{13}\varepsilon_3) + F_{44}C_{44}^2\varepsilon_4^2 + F_{55}C_{55}^2\varepsilon_5^2 + F_{66}C_{66}^2\varepsilon_6^2 = 1 \tag{3}$$

Equation (3) presents the exact expression for the criterion, an intricate formula. The stress-strain correlations in the course of the strain-based Hashin criteria derivation can be expressed as

$\sigma_i = C_{ij}\epsilon_j (i, j = 1, 2, 3, 4, 5, 6)$ . This is a simplified version. As a result, Equation (4) can be written as follows:

$$F_{Tsai} = F_1^\epsilon \epsilon_1 + F_2^\epsilon \epsilon_2 + F_3^\epsilon \epsilon_3 + F_{11}^\epsilon \epsilon_1^2 + F_{22}^\epsilon \epsilon_2^2 + F_{33}^\epsilon \epsilon_3^2 + 2F_{12}^\epsilon \epsilon_1 \epsilon_2 + 2F_{23}^\epsilon \epsilon_2 \epsilon_3 + 2F_{31}^\epsilon \epsilon_3 \epsilon_1 + F_{44}^\epsilon \epsilon_4^2 + F_{55}^\epsilon \epsilon_5^2 + F_{66}^\epsilon \epsilon_6^2 = 1 \tag{4}$$

$$\begin{cases} \epsilon_{1t}^y = \frac{Z_t^y}{C_{11}^y}, \epsilon_{1c}^y = \frac{Z_c^y}{C_{11}^y} \\ \epsilon_{2t}^y = \epsilon_{3t}^y = \frac{X_t^y}{C_{22}^y}, \epsilon_{2c}^y = \epsilon_{3c}^y = \frac{X_c^y}{C_{22}^y}, \\ \gamma_{ij}^y = \frac{S_{ij}^y}{G_{ij}^y} (i, j = 1, 2, 3) \end{cases} \tag{5}$$

where  $F_1^\epsilon = 1/\epsilon_{1t} - 1/\epsilon_{1c}$ ,  $F_2^\epsilon = 1/\epsilon_{2t} - 1/\epsilon_{2c}$ ,  $F_3^\epsilon = 1/\epsilon_{3t} - 1/\epsilon_{3c}$ ,  $F_{11}^\epsilon = 1/(\epsilon_{1t}\epsilon_{1c})$ ,  $F_{22}^\epsilon = 1/(\epsilon_{2t}\epsilon_{2c})$ ,  $F_{33}^\epsilon = 1/(\epsilon_{3t}\epsilon_{3c})$ ,  $F_{44}^\epsilon = 1/(\gamma_{23})^2$ ,  $F_{55}^\epsilon = 1/(\gamma_{31})^2$ ,  $F_{66}^\epsilon = 1/(\gamma_{12})^2$ ,  $F_{12}^\epsilon = -\frac{1}{2}\sqrt{F_{11}^\epsilon F_{22}^\epsilon}$ ,  $F_{23}^\epsilon = -\frac{1}{2}\sqrt{F_{22}^\epsilon F_{33}^\epsilon}$ , and  $F_{31}^\epsilon = -\frac{1}{2}\sqrt{F_{33}^\epsilon F_{11}^\epsilon}$ . Parameters  $\epsilon_{1t}, \epsilon_{1c}, \epsilon_{2t}, \epsilon_{2c}, \epsilon_{3t}, \epsilon_{3c}, \gamma_{23}, \gamma_{31}$ , and  $\gamma_{12}$  are the damage strains for the interwoven composites, which are derivable by Equation (5).

Equation (4) can generate similar results to Equation (3). The form is similar to the form obtained using the Tsai-Wu criterion and in line with the stress value. Hence, Equation (4) was used for the analysis.

The Tsai-Wu criterion cannot be used to differentiate between the failure modes, increasing the difficulty of driving the damaged stiffness matrix. We have defined the three damage mode factors expressed as  $M_1, M_2$ , and  $M_3$  for determining the failure mode. This can be indicated as follows:

$$\begin{cases} M_1 = F_1^\epsilon \epsilon_1 + F_{11}^\epsilon \epsilon_1^2 \\ M_2 = F_2^\epsilon \epsilon_2 + F_{22}^\epsilon \epsilon_2^2 \\ M_3 = F_3^\epsilon \epsilon_3 + F_{33}^\epsilon \epsilon_3^2 \end{cases} \tag{6}$$

When Equation (4) is fulfilled ( $F_{Tsai} > 1$ ), the damage pattern will be identified by utilizing relevant parameters in Equation (6). As an example, in case the absolute  $M_1$  value is the maximum of the three parameters, the failure direction of the material will be along X. Besides, the damage variable can be acquired based on the exponential damage evolution law (Table 1). In Table 1,  $G_c$  is the fracture energy of the braided composites.

**Table 1.** Damage model of the satin weave composites.

| Damage Mode | Maximum Damage Mode Factor                                     | Murakami’s Damage Tensor   |
|-------------|--|--|
| X-direction | $M_1 = F_1^\epsilon \epsilon_1 + F_{11}^\epsilon \epsilon_1^2$ | $d_1 = 1 - \frac{1}{F_{Tsai}} e^{-Z_t \epsilon_1 L^c (F_{Tsai} - 1) / G_c} (\epsilon_1 > 0)$ or $d_1 = 1 - \frac{1}{F_{Tsai}} e^{-Z_c \epsilon_{1c} L^c (F_{Tsai} - 1) / G_c} (\epsilon_1 < 0)$ .<br>$d_2 = d_3 = 0$ |
| Y-direction | $M_2 = F_2^\epsilon \epsilon_2 + F_{22}^\epsilon \epsilon_2^2$ | $d_2 = 1 - \frac{1}{F_{Tsai}} e^{-X_t \epsilon_2 L^c (F_{Tsai} - 1) / G_c} (\epsilon_2 > 0)$ or $d_2 = 1 - \frac{1}{F_{Tsai}} e^{-X_c \epsilon_{2c} L^c (F_{Tsai} - 1) / G_c} (\epsilon_2 < 0)$<br>$d_1 = d_3 = 0$   |
| Z-direction | $M_3 = F_3^\epsilon \epsilon_3 + F_{33}^\epsilon \epsilon_3^2$ | $d_3 = 1 - \frac{1}{F_{Tsai}} e^{-Y_t \epsilon_3 L^c (F_{Tsai} - 1) / G_c} (\epsilon_3 > 0)$ or $d_3 = 1 - \frac{1}{F_{Tsai}} e^{-Y_c \epsilon_{3c} L^c (F_{Tsai} - 1) / G_c} (\epsilon_3 < 0)$ ,<br>$d_1 = d_2 = 0$ |

The damaged stiffness matrix is deduced based on the Murakami damage model [27]. Murakami’s damage tensor,  $\mathbf{D}$ , is expressed as follows:

$$\mathbf{D} = \sum d_i \mathbf{n}_i \otimes \mathbf{n}_i, (i = 1, 2, 3), \tag{7}$$

where  $d_i$  is the damage parameter and  $\mathbf{n}_i$  stands for a principal unit vector matching the damage tensor. Subsequently, the valid stress tensor,  $\sigma$ , was incorporated. Meanwhile, the variable linked to  $\sigma$  is as follows:

$$\sigma = \frac{1}{2} [(\mathbf{I} - \mathbf{D})^{-1} \cdot \sigma + \sigma \cdot (\mathbf{I} - \mathbf{D})^{-1}] = \mathbf{M}(\mathbf{D}) : \sigma \tag{8}$$

where  $\mathbf{I}$  refers to the second-order unit tensor and  $\mathbf{M}(\mathbf{D})$  denotes a fourth-order tensor, which can be deduced in matrix form as follows:

$$\mathbf{M}(\mathbf{D}) = \text{diag} \left\{ \frac{1}{1-d_1}, \frac{1}{1-d_2}, \frac{1}{1-d_3}, \frac{(1-d_1)+(1-d_2)}{2(1-d_1)(1-d_2)}, \frac{(1-d_3)+(1-d_2)}{2(1-d_3)(1-d_2)}, \frac{(1-d_1)+(1-d_3)}{2(1-d_1)(1-d_3)} \right\} \tag{9}$$

In accordance with the Cordebois–Sidoroff hypothesis of energy, we express the equivalence strain energy,  $W_d$ , for the failed material as shown below:

$$W_d = \frac{1}{2} (\sigma)^T : \mathbf{C}^{-1} : \sigma = \frac{1}{2} \sigma^T : \mathbf{M}^T(\mathbf{D}) : \mathbf{C}^{-1} : \mathbf{M}(\mathbf{D}) : \sigma = \frac{1}{2} \sigma^T : \mathbf{C}_d^{-1} : \sigma \tag{10}$$

The damage stiffness matrix can be expressed as follows:

$$\mathbf{C}_d = \mathbf{M}^{-1}(\mathbf{D}) : \mathbf{C} : \mathbf{M}^T(\mathbf{D}) \tag{11}$$

As shown in the matrix form,  $\mathbf{C}_d$  is expressed as follows:

$$\mathbf{C}_d = \begin{bmatrix} b_1^2 C_{11} & b_1 b_2 C_{12} & b_1 b_3 C_{13} & & & & \\ & b_2^2 C_{22} & b_2 b_3 C_{23} & & & & \\ & & b_3^2 C_{33} & & & & \\ & & & b_{23} C_{44} & & & \\ & sym & & & b_{13} C_{55} & & \\ & & & & & b_{12} C_{66} & \end{bmatrix}, \tag{12}$$

where  $b_1 = 1 - d_1$ ,  $b_2 = 1 - d_2$ ,  $b_3 = 1 - d_3$ ,  $b_{23} = (2(1 - d_2)(1 - d_3) / (2 - d_2 - d_3))^2$ ,  $b_{13} = (2(1 - d_1)(1 - d_3) / (2 - d_1 - d_3))^2$ , and  $b_{12} = (2(1 - d_1)(1 - d_2) / (2 - d_1 - d_2))^2$ .

Through alteration of the damage parameters into those in Equation (12), a reduction of stiffness in the 3D interwoven composites is possible. The properties presented in Tables 2 and 3 were used for modeling the behavior of the five-harness satin weave SiC<sub>f</sub>/SiC composites used in the simulations.

**Table 2.** Mechanical properties of the SiC<sub>f</sub>/SiC composites [28].

| $E_X$ (GPa) | $E_Y$ (GPa) | $E_Z$ (GPa) | $\nu_{XY}$ | $\nu_{XZ} = \nu_{YZ}$ | $G_{XY}$ (GPa) | $G_{XZ} = G_{YZ}$ (GPa) |
|-------------|-------------|-------------|------------|-----------------------|----------------|-------------------------|
| 51.031      | 50.751      | 10.53       | 0.31       | 0.42                  | 4.36           | 3.048                   |

**Table 3.** Strength and damage data corresponding to the SiC<sub>f</sub>/SiC composites.

| Strength    | $X_T$ (MPa)              | $Y_T$ (MPa)              | $S_{XY}$ (MPa)  | $S_{YZ}$ (MPa)  |
|-------------|--------------------------|--------------------------|-----------------|-----------------|
| [29]        | $X_C$ (MPa)              | $Y_C$ (MPa)              | $S_{XZ}$ (MPa)  |                 |
|             | 754                      | 734                      | 56              | 56              |
|             | 618                      | 621                      | 56              |                 |
| Damage [30] | $G_{Xt} = G_{Yt}$ (N/mm) | $G_{Xc} = G_{Yc}$ (N/mm) | $G_{Zt}$ (N/mm) | $G_{Zc}$ (N/mm) |
|             | 8                        | 1.5                      | 0.632           | 0.306           |

### 3.3. The Traction–Separation Damage Law

The interface debonding in the five-harness satin weave composite plates is an important damage mode, and the interfacial simulation is accomplished with the cohesive

element, whose failure behavior is elucidated often by the bilinear pattern (Figure 5). In the model, there are three interfacial failure modes, with Mode N representing the tensile failure, whereas Modes S and T represent the shear failure.

As presented in Figure 6,  $t_i$  ( $i = N, S, T$ ) denotes the traction stress,  $\delta_i$  refers to the separation displacement, while  $t_i^0$  and  $\delta_i^0$  separately denote the initial damage stress and displacement. These parameters are expressed as follows:

$$\delta_i^0 = \frac{t_i^0}{k_i} (i = N, S, T), \tag{13}$$

where  $k_i$  indicates the stiffness of the interface in the  $i$  direction.

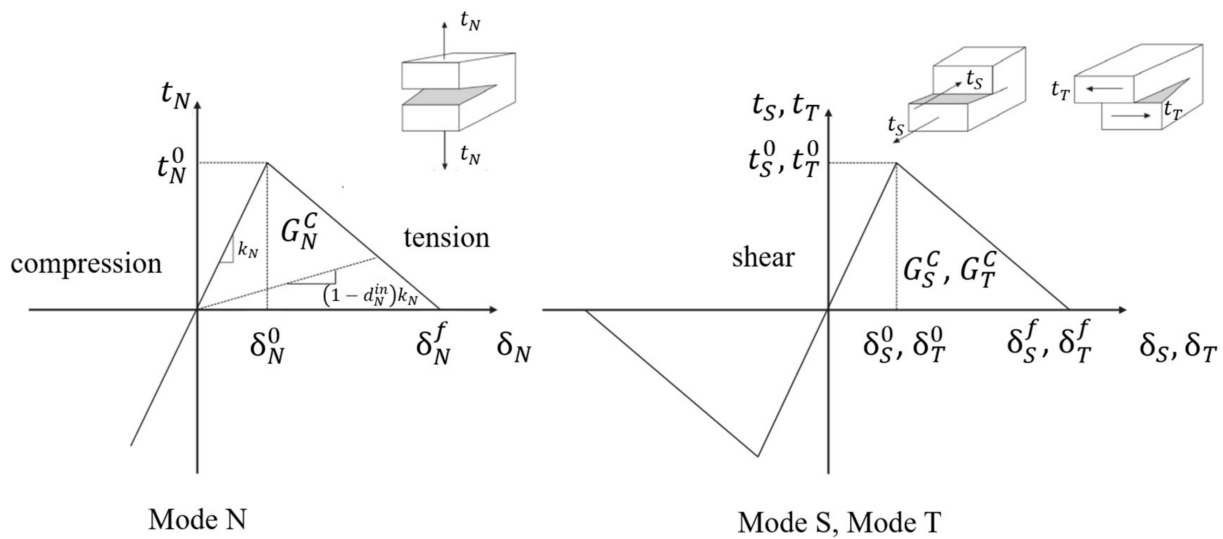


Figure 6. Delamination mode of the cohesive model.

In Figure 5,  $\delta_i^f$  indicates the deformation for full debonding, whereas  $G_i^C$  stands for the fracture energy. The following equation can be obtained based on the definition of  $G_i^C = \int_0^{\delta_i^f} t_i d\delta_i$ :

$$\delta_i^f = \frac{2G_i^C}{t_i^0} (i = N, S, T) \tag{14}$$

When traction displacement,  $\delta_i$ , reaches  $\delta_i^0$ , the damage propagates. The damage variable can be expressed as follows:

$$d_i^{in} = \frac{\delta_i^f (\delta_i - \delta_i^0)}{\delta_i (\delta_i^f - \delta_i^0)}, 0 \leq d_i^{in} \leq 1 (i = N, S, T), \tag{15}$$

where the superscript 'in' denotes the interface. The expression for the failed interfacial constitutive model is shown below:

$$t_i = (1 - d_i^{in}) k_i \delta_i, \delta_i^0 \leq \delta_i \leq \delta_i^f (i = N, S, T), \tag{16}$$

where it is assumed that Mode N and Mode T share an identical stiffness coefficient, fracture energy, as well as damage initiation [31]. Moreover, Mode N shares an identical stiffness coefficient with the other two Modes, i.e.,  $t_S^0 = t_T^0$ ,  $G_S^C = G_T^C$  and  $k_S = k_T = k_N = K$ .

Based on the above discussion, it can be hypothesized that the failure model is based on a unitary mode. Under real scenarios, the mode of failure will probably be hybrid. Besides, the expression for separation deformation of the combinatory mode,  $\delta_m$ , is shown below:

$$\delta_m = \sqrt{\langle \delta_1 \rangle^2 + \delta_2^2 + \delta_3^2} = \sqrt{\langle \delta_1 \rangle^2 + \delta_{\text{shear}}^2}, \tag{17}$$

where  $\delta_{\text{shear}}$  refers to the norm of the vector defining the tangential relative displacement. We can deduce the  $\langle \cdot \rangle$  operator as follows:

$$\langle x \rangle = \begin{cases} 0, & x \leq 0 \\ x, & x > 0 \end{cases} \tag{18}$$

The initial failure for the combinatory mode is validated by utilizing the criterion of quadratic nominal stress. The expression is as follows:

$$\left( \frac{\langle t_N \rangle}{t_N^0} \right)^2 + \left( \frac{\langle t_S \rangle}{t_S^0} \right)^2 + \left( \frac{\langle t_T \rangle}{t_T^0} \right)^2 = 1 \tag{19}$$

By substituting Equations (14) and (17) into (19) and solving for  $\delta_m$ , we obtain Equation (20) as follows:

$$\delta_m^0 = \begin{cases} \delta_N^0 \delta_{\text{shear}}^0 \sqrt{\frac{1+\beta^2}{(\delta_{\text{shear}}^0)^2 + (\beta \delta_{\text{shear}}^0)^2}}, & \delta_N > 0 \\ \delta_{\text{shear}}^0, & \delta_N \leq 0 \end{cases}, \tag{20}$$

where  $\beta$  indicates the ratio between the tensile and shear deformations (i.e.,  $\beta = \delta_{\text{shear}} / \delta_N$  and  $\delta_{\text{shear}}^0 = \delta_S^0 = \delta_T^0$ ).

The failure deformation for the combinatory mode,  $\delta_m^f$ , is expressed from the B-K criterion:

$$\delta_m^f = \begin{cases} \frac{2}{K \delta_m^0} \left[ G_N^C + (G_S^C - G_N^C) \left( \frac{\beta^2}{1+\beta^2} \right)^\eta \right], & \delta_N > 0 \\ \sqrt{(\delta_S^f)^2 + (\delta_T^f)^2}, & \delta_N \leq 0 \end{cases} \tag{21}$$

In addition, Equations (15) and (16) can separately serve as the governing equations for the failure evolution and constitutive model of the combinatory mode (the *i*-to-*bm* modification of subscripts in these two equations is necessary).

Table 4 summarizes the material parameters used for the analysis.

**Table 4.** Interface properties of the five-harness SiC<sub>f</sub>/PyC/SiC satin weave composites [32].

|                |     |                        |     |
|----------------|-----|------------------------|-----|
| $t_N^0$ (MPa)  | 45  | $t_S^0 = t_T^0$ (MPa)  | 35  |
| $G_N^C$ (N/mm) | 0.3 | $G_S^C = G_T^C$ (N/mm) | 1.0 |

Besides, the mass scaling factor was assigned as  $10^3$  by consulting [33], so that the computation was more efficient while ensuring the accuracy.

### 3.4. Mesh Convergence Validation

Mesh quality is an essential factor in forecasting accuracy. The mesh was selected by consulting the refinement analysis outcomes. The model’s normalized bending moduli of elasticity were considered, and divided by the effective model moduli with an approximately 0.4 mm size of elements. The size of the elements was 0.4, 0.3, 0.2, and 0.15 mm, respectively. Figure 7 shows the restricted changes (less than 2%) of the normalized moduli for different meshes. The local diagrams exhibit the changes in the meshed models with changes in the element size. No significant change in the trends and outcomes was

found as the meshes were further refined. Consistent results were obtained. The computational duration increased significantly with a decrease in the mesh size. The element size was finally set at 0.2 mm following a trade-off between the calculation accuracy and the computational cost.

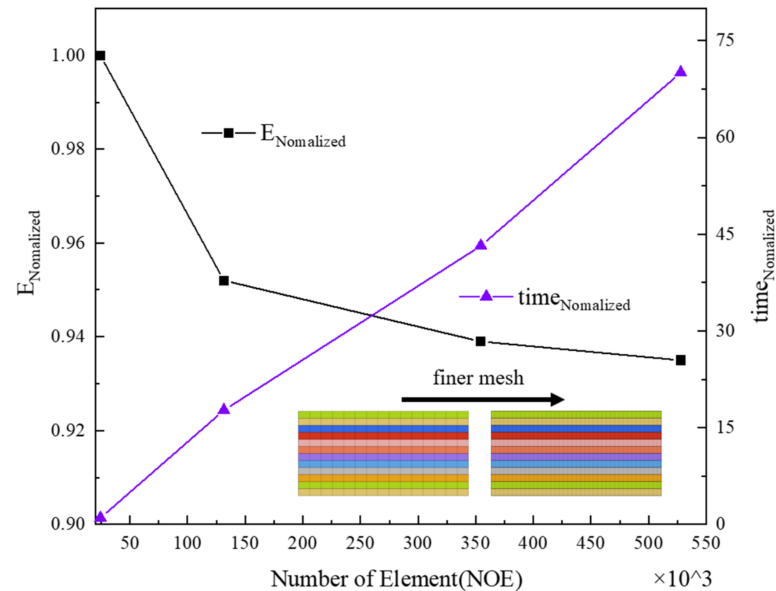


**Figure 7.** Normalized moduli and computing time as a function of element number.

#### 4. Results and Discussion

In the following section, the failure mechanisms will be explored for the SiC<sub>f</sub>/PyC/SiC satin weave composite plates. During the material behavior assessment, we utilized the numerically and experimentally generated load–displacement graphs, damage variable fields corresponding to the model, electron microscopic view of composite fracture, and surface strain fields of the samples.

According to the experimental standard [34], Figure 8 presents the load–deformation graphs derived both numerically and experimentally. The curves were generated by conducting the three-point bending tests with the SiC<sub>f</sub>/PyC/SiC composites. As the constitutive law explained nonlinearity effects, the predictions based on the established numerical model were favorably consistent with the outcomes of experimentation. Since the composite material possesses outstanding mechanical properties, the sample could bear the load at larger displacements. The nonlinearity in the woven material features the relative reorientation of warp and weft lines. The PyC interface layer helps hinder the development of main cracks, which are generated from the microcracks from the matrix. The fiber fracture of the SiC<sub>f</sub>/SiC composite was observed, and the continuous evolution of such damage subjected to loading stresses caused delamination. Such behavior is assumed to be of the ‘ductile nonlinear’ type.

Figure 9 presents the SEM images of the SiC<sub>f</sub>/PyC/SiC composites. According to Figure 9A, there exists an obvious PyC interface between the fibers and matrix, and no obvious gap was observed between the two. In the load process of the composite, the cracks originating from the current micropores of the composite material subsequently formed large cracks. Due to the laminar structure on the PyC interface, the deflection effect occurred on the cracks, and the cracks then expanded on the interface. Under these conditions, a certain amount of strain energy was dissipated, and the formation of fiber fracture was delayed. Figure 9B,C show that the fiber was obviously pulled out at the fracture of the composite material, which indicates that fiber fracture is the main failure mode of the material.

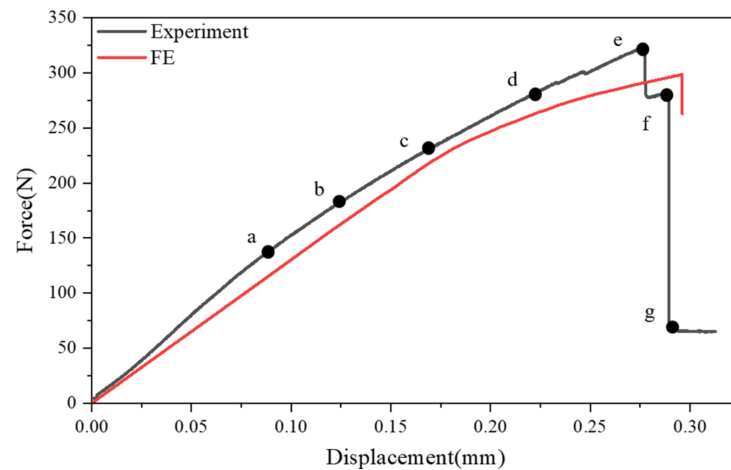


**Figure 8.** Experimental and numerical force–displacement curves.

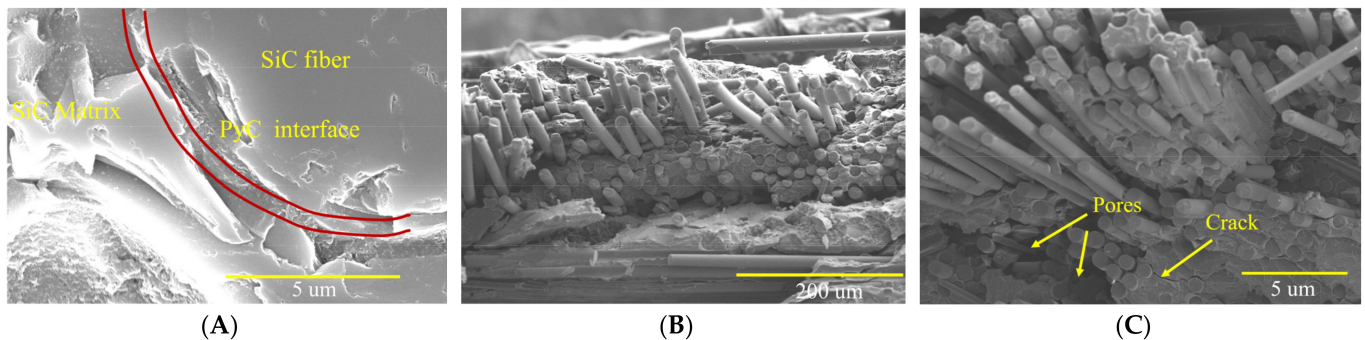
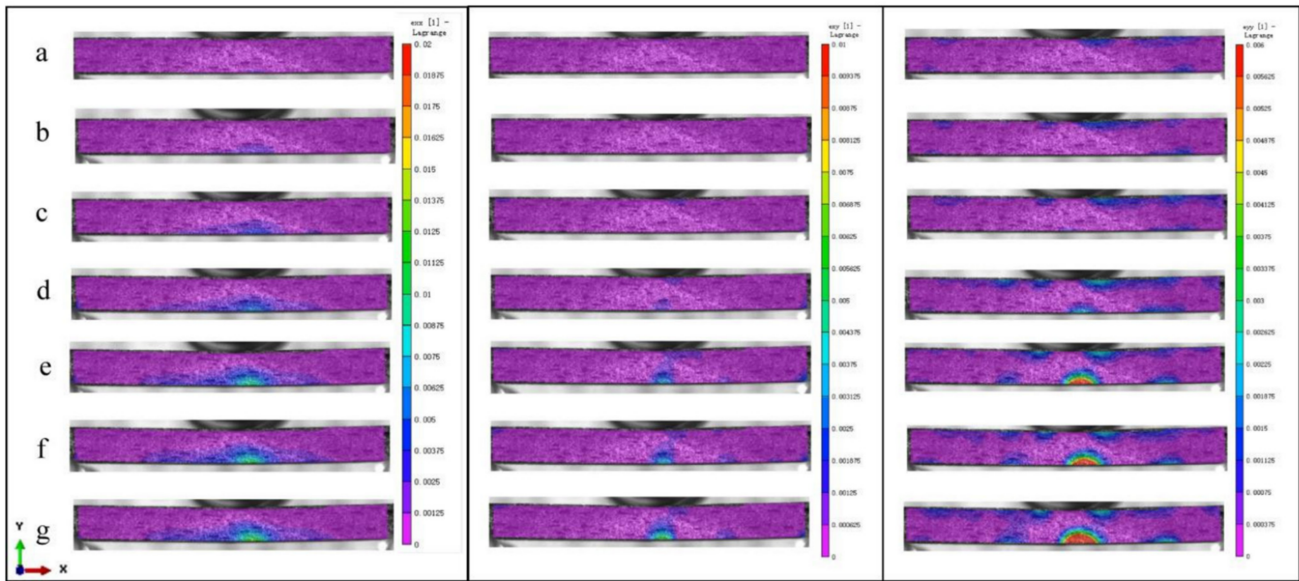


**Figure 9.** SEM images of the SiC<sub>f</sub>/PyC/SiC composites. (A) Interface, (B) fracture morphology, and (C) fiber pulling out.

The extraction of the strain distributions on the surface of specimens was completed using the recorded images. Figure 10 presents the full-field  $\varepsilon_{xx}$ ,  $\varepsilon_{yy}$ , and  $\varepsilon_{xy}$  strain contours subjected to forces of magnitude 135, 181, 227, 272, 323, 280, and 64 N. These correspond to letters a–g, as seen in Figure 8. Figure 10 presents the regular change in the strain distributions on the satin-woven composite surface. Since the value of  $\varepsilon_{xx}$  exceeds that of  $\varepsilon_{yy}$  and  $\varepsilon_{xy}$  in strain distribution acquired by DIC,  $x$ -directional tensile damage dominates the damage mode in the specimen. For composites under the damage extension mode, the  $x$ -directional tensile strain at the bottom of the specimen propagated rapidly until complete failure of the material was achieved. Microcracks appeared and propagated on the composite surface, and this can be attributed to the low-strength and high matrix strain, as displayed in Figure 10. The cracks of the matrix also indicate the yarn micro-failure of the composites. Affected by reduced load capacity in failed yarns and transfer of loads to the neighboring matrix, the stress in the matrix was increased, initiating the formation of the cracks. Under the load of approximately 270 N, the cracks occurred at different matrix sites and then spread, resulting in the generation of a primary crack and sample fractures. As the load intensified, a main crack was generated from minor cracks (nucleation of cracks). Fiber fracturing should appear when stress approaches the strength. Under conditions of stress less than 230 N, no significant cracks were found to form on the surface. In the presence of the interface, the process of fiber damage proceeds over multiple steps instead of a sudden fracture step. This results in the generation of pseudoplastic traits in the composites.



(A) (B) (C)

**Figure 10.** Evolution of the full-field strains under the forces of 135, 181, 227, 272, 323, 280, and 64 N: (A)  $\epsilon_{xx}$ , (B)  $\epsilon_{yy}$ , and (C)  $\epsilon_{xy}$ .

Figure 11 presents the specimen surface distribution of  $\epsilon_{xx}$  (SDV10 represents  $\epsilon_{xx}$ ). This can be acquired from FE simulations. The lower side of the specimen was exposed to tensile strain, and the upper side was exposed to compressive strain attributable to the three-point bending mode associated with the composite. Based on the mappings, large-area deformation on the material surface was determined. The results agree well with the strain distribution determined following the DIC approach (Figure 10). Due to the presence of the PyC interface layer, the strains on the specimen surface should be centralized within a limited range. This suggests that a PyC interface characterized by proper stiffness can limit deformation in a small scope. A satisfactory connection between the tested and expected failure locations may be obtained.

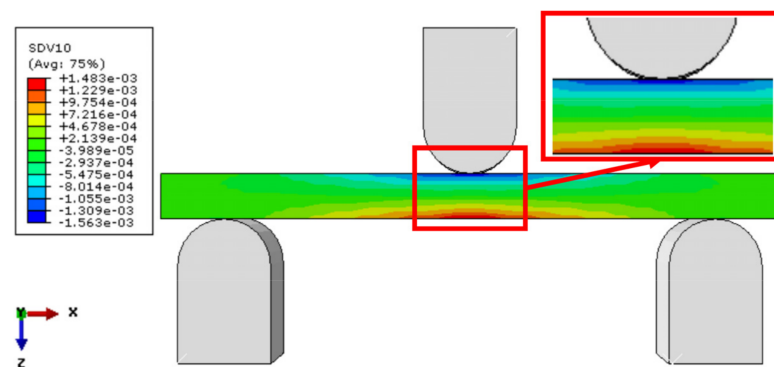


**Figure 11.** The  $\epsilon_{xx}$  on the sample surface.

Figure 12 presents the distribution of the damage mode factors on the sample surface obtained from FE simulations (SDV8 represents damage mode factors). The damage mode factors can determine the damage mode of the FE model during the loading process. The lower and upper sides of the specimen were both reflected by the X-directional damage model. The three-point bending rule can be applied to the sample. The mappings are consistent with the strain distribution determined using the DIC approach (Figure 10). The distribution of  $\epsilon_{xx}$  on the sample surface is presented in Figure 11.

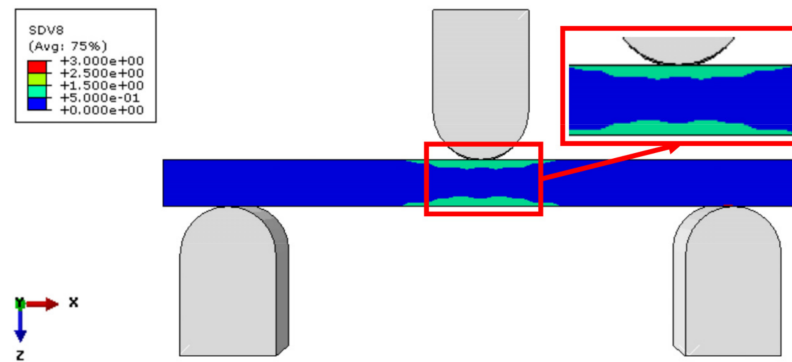


Figure 12. Damage mode factors on the sample surface.

The distribution of the compressive and tensile composite failures on the specimen is illustrated in Figure 13 (SDV1 and SDV2 represent tensile and compression damage). Tensile damage was the predominant mode of material failure on the lower side, while compressive damage was the predominant mode of failure on the upper side. The former is ascribed to the tensile strain imposed primarily on the lower side, whereas the latter is ascribed to the compressive strain imposed primarily on the upper portion of the specimen. As evident from the local plots, during the crossing of varying layups, the degrees of compressive and tensile damage significantly decreased. This can be attributed to the certain impedance of damage propagation by the PyC interfacial layer. The minor cracks (that caused fiber disruption) associated with the primary mechanism were deflected by adequate interfacial strength. This pushed the major cracks backward, and the material failure process was postponed, resulting in pseudoplasticity.

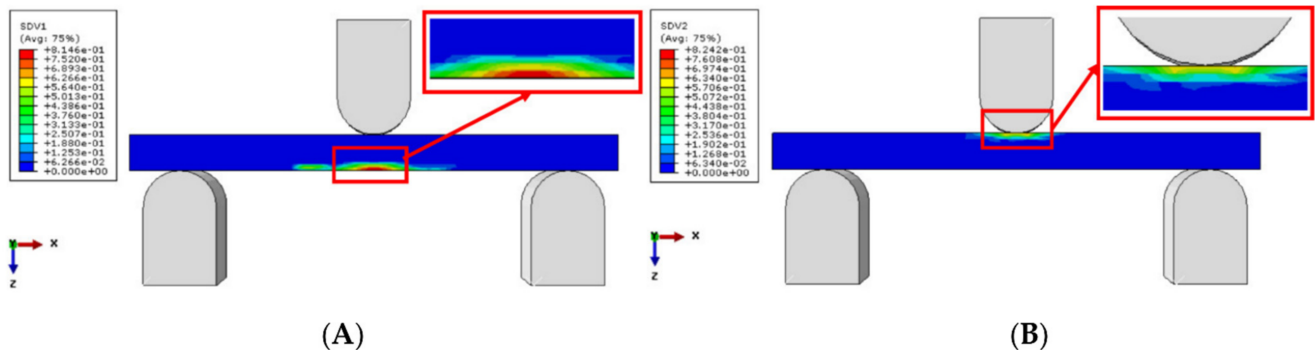
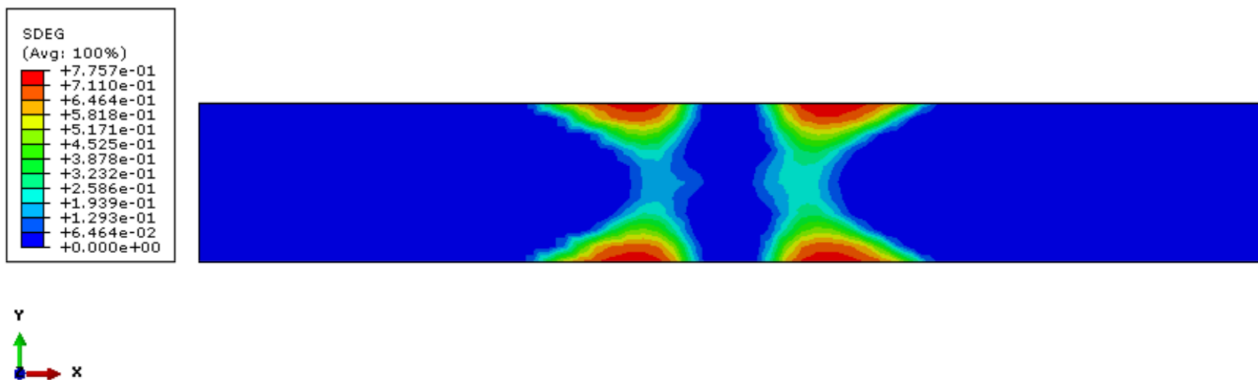


Figure 13. Distribution of the damage variable fields. (A) Tension damage and (B) compression damage.

According to Figure 14, due to the free edge effect, the damages of the interface first appeared at the edge of the specimen. Subsequently, the interfacial damage continued to progress until the interface delaminated. In the general stress state, the composite laminate presents a certain free edge impact, which is usually denoted as the stress concentration. This makes the delamination damage appear in the composite, the strength of which is significantly lower than the service strength. This results in the early failure of the composite. Consequently, the damage value of the interface at the free edge is the maximum under these conditions. Nevertheless, the cracks were deflected due to the effect of the PyC interface with the proper interface stiffness and strength. This can delay the process of formation of the primary cracks. It can also enhance the damage tolerance of the specimens. Thus, it was observed that the SiC<sub>f</sub>/PyC/SiC satin weave composite plates presented specific pseudoplastic characteristics. Delamination was proven as the efficient toughening mechanism in which the fracture energy can dissipate at the cost of cracking.



**Figure 14.** Distribution of damage variable fields on the PyC interface.

## 5. Conclusions

In this three-point bending test-based study, we explored the failure behavior of five-harness  $\text{SiC}_f/\text{PyC}/\text{SiC}$  satin-woven sheet composites consisting of twelve layers using a combination of numerical and experimental methods. For the interpretation of damage initiation and progression in these composites, the DIC approach was adopted. Conclusions were drawn as follows:

1. The three-point bending procedure was implemented on the five-harness satin-woven  $\text{SiC}_f/\text{PyC}/\text{SiC}$  composite for later application into the developed FE model. The material behavior was mimicked based on the modified 3D Tsai-Wu theory that was executed following the VUMAT subroutine. A favorable agreement was found between the simulation and experimental results in terms of both the load–deformation graphs and the strain fields (the strength value error was less than 10%). Compared with [35], the force–displacement curve of the composite became smoother as the number of layers increased.
2. The duration of failure accumulation prior to the generation of full composite damage was prolonged due to the presence of the PyC interface. This also prolonged the duration of the material failure warning, enhanced the safety of composite application, and broadened its application scope.
3. In an intricate stress state, a certain free edge effect was observed in the presence of an interfacial layer. Even though different layers of the composite exhibited similar mechanical performance, enrichment of stresses was also observed. Due to the effect of the free edge, the composite will undergo delamination failure, and its bearing potential will be compromised, resulting in premature composite damage.
4. Compared with the Hashin criterion in [35], the failure mode factors were more accurately suggestive of the chief mode of composite damage in a 3D stress state. In the case of the satin-woven composite studied here, the failure mechanism involved fiber pulling out and matrix cracking.
5. Each layer of the five-harness, twelve-layer satin-woven composite material is considered homogeneous and anisotropic, so it was hard to obtain the effect of the meso-structure on the composite; therefore, mesoscopic models can be further exploited to quantify the effect.

**Author Contributions:** Writing—review and editing, X.L.; supervision, R.L. All authors have read and agreed to the published version of the manuscript.

**Funding:** This research received no external funding.

**Institutional Review Board Statement:** Not applicable.

**Informed Consent Statement:** Not applicable.

**Data Availability Statement:** Data available on request form the authors.

**Conflicts of Interest:** The authors declare no conflict of interest.

## References

1. Dalmaz, A.; Ducret, D.; El Guerjouma, R.; Reynaud, P.; Franciosi, P.; Rouby, D.; Fantozzi, G.; Baboux, J.C. Elastic moduli of a 2.5D Cf/SiC composite: Experimental and the oretical estimates. *Compos. Sci. Technol.* **2000**, *60*, 913–925. [[CrossRef](#)]
2. Chen, S.; Fei, Q.; Jiang, D.; Cao, Z. Determination of thermo-elastic parameters for dynamical modeling of 2.5D C/SiC braided composites. *J. Mech. Sci. Technol.* **2018**, *32*, 231–243. [[CrossRef](#)]
3. Wang, Y.; Zhang, L.; Cheng, L.; Ma, J.; Zhang, W. Tensile performance and damage evolution of a 2.5-D C/SiC composite characterized by acoustic emis-sion. *Appl. Compos. Mater.* **2008**, *15*, 183–188. [[CrossRef](#)]
4. Wan, Y.; Zak, G.; Naumann, S.; Redekop, S.; Slywynska, I.; Jiang, Y. Study of 2.5-D glass-fabric-reinforced light-curable resin composites for orthotic applications. *Compos. Sci. Technol.* **2007**, *67*, 2739–2746. [[CrossRef](#)]
5. Hallal, A.; Younes, R.; Fardoun, F.; Nehme, S. Improved analytical model to predict the effective elastic properties of 2.5D interlock woven fabrics composite. *Compos. Struct.* **2012**, *94*, 3009–3028. [[CrossRef](#)]
6. Daggumati, S.; Van Paepegem, W.; Degrieck, J.; Xu, J.; Lomov, S.V.; Verpoest, I. Local damage in a 5-harness satin weave com-posite under static tension: Part II–Meso-FE modelling. *Composites Sci. Technol.* **2010**, *70*, 1934–1941. [[CrossRef](#)]
7. Zako, M.; Uetsuji, Y.; Kurashiki, T. Finite element analysis of damaged woven fabric composite materials. *Compos. Sci. Technol.* **2003**, *63*, 507–516. [[CrossRef](#)]
8. Guo-Dong, F.; Jun, L.; Bao-Lai, W. Progressive damage and nonlinear analysis of 3D four-directional braided composites under unidirectional tension. *Compos. Struct.* **2009**, *89*, 126–133. [[CrossRef](#)]
9. Hühne, C.; Zerbst, A.-K.; Kuhlmann, G.; Steenbock, C.; Rolfes, R. Progressive damage analysis of composite bolted joints with liquid shim layers using constant and continuous degradation models. *Compos. Struct.* **2010**, *92*, 189–200. [[CrossRef](#)]
10. Abbassi, F.; Mistou, S.; Zghal, A. Failure analysis based on microvoid growth for sheet metal during uniaxial and biaxial tensile tests. *Mater. Des.* **2013**, *49*, 638–646. [[CrossRef](#)]
11. Zhang, C.; Li, N.; Wang, W.; Binienda, W.K.; Fang, H. Progressive damage simulation of triaxially braided composite using a 3D meso-scale finite element model. *Compos. Struct.* **2015**, *125*, 104–116. [[CrossRef](#)]
12. Doitrand, A.; Fagiano, C.; Chiaruttini, V.; Leroy, F.; Mavel, A.; Hirsekorn, M. Experimental characterization and numerical modeling of damage at the mesoscopic scale of woven polymer matrix composites under quasi-static tensile loading. *Compos. Sci. Technol.* **2015**, *119*, 1–11. [[CrossRef](#)]
13. Lisle, T.; Bouvet, C.; Pastor, M.; Margueres, P.; Corral, R.P. Damage analysis and fracture toughness evaluation in a thin woven composite laminate under static tension using infrared thermography. *Compos. Part A Appl. Sci. Manuf.* **2013**, *53*, 75–87. [[CrossRef](#)]
14. D’Haen, J.J.A.; May, M.; Knoll, O.; Kerscher, S.; Hiermaier, S. Strain Acquisition Framework and Novel Bending Evaluation Formulation for Compression-Loaded Composites Using Digital Image Correlation. *Materials* **2021**, *14*, 5931. [[CrossRef](#)]
15. Zhang, Z.; Li, L.; Chen, Z. Damage Evolution and Fracture Behavior of C/SiC Minicomposites with Different Interphases under Uniaxial Tensile Load. *Materials* **2021**, *14*, 1525. [[CrossRef](#)]
16. Zhang, Y.; Zhou, Z.; Tan, Z. Compression Shear Properties of Bonded–Bolted Hybrid Single-Lap Joints of C/C Composites at High Temperature. *Appl. Sci.* **2020**, *10*, 1054. [[CrossRef](#)]
17. De Domenico, D.; Quattrocchi, A.; Alizzio, D.; Montanini, R.; Urso, S.; Ricciardi, G.; Recupero, A. Experimental Characterization of the FRCM-Concrete Interface Bond Behavior Assisted by Digital Image Correlation. *Sensors* **2021**, *21*, 1154. [[CrossRef](#)]
18. Li, K.; Kashkarov, E.; Ma, H.; Fan, P.; Zhang, Q.; Zhang, P.; Zhang, J.; Wu, Z.; Wahl, L.; Laptev, R.; et al. Microstructural Analysis of Novel Pre-ceramic Paper-Derived SiC<sub>f</sub>/SiC Composites. *Materials* **2021**, *14*, 6737. [[CrossRef](#)]
19. Wimmer, G.; Kitzmüller, W.; Pinter, G.; Wettemann, T.; Pettermann, H. Computational and experimental investigation of delamination in L-shaped laminated composite components. *Eng. Fract. Mech.* **2009**, *76*, 2810–2820. [[CrossRef](#)]
20. Fletcher, T.A.; Kim, T.; Dodwell, T.J.; Butler, R.; Scheichl, R.; Newley, R. Resin treatment of free edges to aid certification of through thickness laminate strength. *Compos. Struct.* **2016**, *146*, 26–33. [[CrossRef](#)]
21. Mittelstedt, C.; Becker, W. Free-Edge Effects in Composite Laminates. *Appl. Mech. Rev.* **2007**, *60*, 217–245. [[CrossRef](#)]
22. Gomes, G.F.; Diniz, C.A.; Da Cunha, S.S.; Ancelotti, A.C. Design Optimization of Composite Prosthetic Tubes Using GA-ANN Algorithm Considering Tsai-Wu Failure Criteria. *J. Fail. Anal. Prev.* **2017**, *17*, 740–749. [[CrossRef](#)]
23. Hashin, Z.; Rotem, A. A Fatigue Failure Criterion for Fiber Reinforced Materials. *J. Compos. Mater.* **1973**, *7*, 448–464. [[CrossRef](#)]
24. Hashin, Z. Fatigue Failure Criteria for Unidirectional Fiber Composites. *J. Appl. Mech.* **1981**, *48*, 846–852. [[CrossRef](#)]
25. Puck, A.; Schürmann, H. Failure analysis of FRP laminates by means of physically based phenomenological models. *Compos. Sci. Technol.* **2002**, *62*, 1633–1662. [[CrossRef](#)]
26. Chang, F.-K.; Chang, K.-Y. A Progressive Damage Model for Laminated Composites Containing Stress Concentrations. *J. Compos. Mater.* **1987**, *21*, 834–855. [[CrossRef](#)]
27. Murakami, S. Mechanical Modeling of Material Damage. *J. Appl. Mech.* **1988**, *55*, 280–286. [[CrossRef](#)]
28. Jebri, L.; Abbassi, F.; Demiral, M.; Soula, M.; Ahmad, F. Experimental and numerical analysis of progressive damage and failure behavior of carbon Woven-PPS. *Compos. Struct.* **2020**, *243*, 112234. [[CrossRef](#)]

29. Liang, Y.; Wang, H.; Soutis, C.; Lowe, T.; Cernik, R. Progressive damage in satin weave carbon/epoxy composites under qua-si-static punch-shear loading. *Polym. Test* **2015**, *41*, 82–91. [[CrossRef](#)]
30. Hong, Y.; Yan, Y.; Tian, Z.; Guo, F.; Ye, J. Mechanical behavior analysis of 3D braided composite joint via experiment and multiscale finite element method. *Compos. Struct.* **2018**, *208*, 200–212. [[CrossRef](#)]
31. Zhang, C.; Curiel-Sosa, J.; Bui, T.Q. A novel interface constitutive model for prediction of stiffness and strength in 3D braided composites. *Compos. Struct.* **2017**, *163*, 32–43. [[CrossRef](#)]
32. Chen, J.; Ravey, E.; Hallett, S.; Wisnom, M.; Grassi, M. Prediction of delamination in braided composite T-piece specimens. *Compos. Sci. Technol.* **2009**, *69*, 2363–2367. [[CrossRef](#)]
33. Ducobu, F.; Rivière-Lorphèvre, E.; Filippi, E. On the introduction of adaptive mass scaling in a finite element model of Ti6Al4V orthogonal cutting. *Simul. Model. Pract. Theory* **2015**, *53*, 1–14. [[CrossRef](#)]
34. GB/T 35100-2018; Fiber Metal Laminates—Determination of Interlaminar Shear Strength by Short-Beam Method. China National Standardization Administration: Beijing, China, 2018.
35. Li, X.; Luo, R. Experimental and Numerical Analysis of Progressive Damage of SiC<sub>f</sub>/SiC Composite under Three-Point Bending. *Crystals* **2022**, *12*, 720. [[CrossRef](#)]